Wideband Measurement Based Vehicle to Pedestrian Channel Models

Gloria Makhoul, *Member, IEEE*, Raffaele D'Errico, *Member, IEEE*, Claude Oestges, *Fellow, IEEE*

***Abstract*—This paper presents a vehicle to pedestrian (V2P) channel model based on an extensive measurement campaign carried out at 3.8 GHz. Several propagation conditions were investigated and different mobility patterns were measured. A stochastic channel modeling approach is proposed and parametrized. The model consists of two components, i.e. the first path component and the secondary multi-path components (MPCs). These components were detected via a detection and tracking algorithms presented here. It was found that the time variant contributions of each detected path can be modeled as a combination of path loss (PL), large- and small-scale fading.**

***Index Terms*—Vehicle to pedestrian, propagation, measurement, channel modeling.**

I. Introduction

Vehicle-to-Everything (V2X) communications are defined as a direct link between moving vehicles and a wide set of road passengers like vehicles, pedestrian, bicyclists etc. It has received a significant attention in the recent years for road safety based on intelligent transportation systems (ITS). As a result, the IEEE 802.11p standard was developed for dedicated short range communication (DSRC) [1].

Knowledge of the V2X propagation characteristics is prerequisite for the design, testing and improvement of future road safety communication systems such as crossing street intersections, change or merge land, crash warning etc. [2]. The peculiarity of V2X channels stems from the channel non-stationarity, i.e. the channel statistics can vary over time. This is mainly due to the dynamic change of the environments around both mobile terminals. Two major approaches, that can include this aspect, are the geometry-based stochastic channel model (GSCM) [3], [4] and the tapped delay line (TDL) model including birth/death process to account the appearance and disappearance of taps [5], [6].

While vehicle-to-vehicle (V2V) propagation was largely addressed in the literature, vehicle to pedestrian (V2P) channels have received a poor attention. In [7], the V2P channel statistics at 1.85 GHz were presented considering a moving and stationary person while a stationary person were considered in [8], [9]. Some simulations of V2P and vehicle-to-infrastructure (V2P/I) communication channel performances, i.e. delay and Doppler spreads, at the seaport were investigated at 5.9 GHz in [10] considering front-lifts as vehicles and on port workers as pedestrians. In [11], the received power values extracted from the received signal strength indicator (RSSI) and the Inter Packet Gap (IPG), i.e. the time between successive successful receptions of messages sent by a specific transmitter, have shown that a communication distances of at least 160 m is attainable for line-of-sight (LoS) and non-line-of-sight (NLoS) V2P scenarios. Recently, wide-band V2P channel measurement campaigns were performed using a channel sounder at 5.2 GHz and the ITS-G5 systems [12]. Different scenarios were considered there, i.e. moving/static pedestrian, LoS/NLoS and with/without crowd shadowing and thence, two path loss (PL) models, the log-distance and two ray models, were proposed.

This paper presents a stochastic channel modeling approach for the V2P channels based on measurement campaign carried out at 3.8 GHz. Several propagation conditions and different mobility patterns were investigated. The model is similar to the one proposed in [4] and it consists of first path component and secondary discrete multipath-components (MPCs). In order to track the time evolution of the first path component and the secondary MPCs, a detection procedure and a tracking algorithm were implemented. A parametrization technique was then presented. At this point, it is worth noting that the preliminary results of LoS measurement scenarios were reported for each given mobility pattern in [13].

This paper is organized as follows. The V2P channel measurement campaign is detailed in Section II. Section III presents the proposed channel modeling approach, the first path and the secondary discrete multi-path detection procedure and the tracking algorithm. The parametrization technique for the first path component and the secondary MPCs are described in Section IV. Finally, conclusions are given in Section V.

II. Channel Measurement Campaign

A. Measurement Setup

A V2P measurement campaign was carried out using UCLouvain-ULB channel sounder. The center frequency f_c was 3.8 GHz and the measurement bandwidth B was set to 200 MHz resulting in a high delay resolution of 5 ns. The choice of frequency and bandwidth was driven by the capacity of the channel sounder. Note that the channel model is not too sensitive to the exact frequency in the 1-5 GHz frequency range. The transmit power at the antenna ports was 23 dBm. The code length N_{ch} was 4094 which corresponds to a

G. Makhoul is with CEA-LETI, Minatec Campus, and with Université Grenoble-Alpes, both in Grenoble, France.

R. D'Errico is with CEA-LETI, Minatec Campus and with Université Grenoble-Alpes, both in Grenoble, France.

C. Oestges is with the ICTEAM Institute, Université catholique de Louvain, Louvain-la-Neuve, Belgium.

This work was carried out within COST Action CA15104 IRACON and it was partially funded by ANR project MoreOVer.

Manuscript received XXX, XX, 2018; revised XXX, XX, 2018.

maximum measurable excess delay τ_{excess} of 20.47 μs giving rise to a maximum measurable path length of 6.141 km. To achieve a high Doppler resolution, a channel sampling rate ν_{cs} of 1062 Hz was considered which corresponds to a maximum relative speed of 150 km/h approximately. The main channel sounder parameters are summarized in Table I.

During measurements, the channel sounder stored the transmitter (Tx) location by a GPS together with the measured data stream (time-tagged).The GPS has a frequency resolution of 1 Hz (a location record each 1 s) and a positioning errors ranging from 2 m to 10 m, approximately. The World Geodetic System (WGS 84) was used to determine the GPS records. Therefore, the accuracy, with which the orbit is predicted, is typically at the few meter level. This is not precise enough for range measurements that must satisfy the requirements of cm level GPS positioning. However, in our case, this accuracy is considered as sufficient because the measurement bandwidth was 200 MHz which corresponds to a distance resolution of 1.5 m. Note that the GPS vehicular location is out of scope of this paper.

TABLE I: Measurement setup parameters

Center frequency f_c	3.8 GHz
Bandwidth B	200 MHz
Delay resolution	5 ns
Frequency spacing	48.85 KHz
Transmit power	23 dBm
code length N_{ch}	4094
Maximum measurable excess delay, τ_{excess}	20.47 μs
Channel sampling rate ν_{cs}	1062 Hz
Time resolution	941.62 μs

Dipole antennas were used at Tx and receiver (Rx) terminals. Tx antenna was mounted on the roof of a car while the Rx antenna was placed on a cardboard tube carried by a human subject acting as a pedestrian (cf. Fig. 1). At this point, it is worth noting that a variation in antenna height may impact the propagation signal due to the low antenna heights [14]. In our measurement, the Tx antenna height was approximately 1.7 m while the Rx antenna height was around 1 m. The following proposed model can be further extended by studying the height effect on the propagation channel signal. This requires further investigation and it is beyond the scope of this paper.

(a) LoS measurement (b) Partial LoS measurement

Fig. 1: Example of LoS and partial LoS measurements

B. Measurement Scenarios

Our V2P measurement campaign was carried out in two different site locations. Fig. 2 presents satellite photographs of the measurement sites where the red lines indicate Tx path.

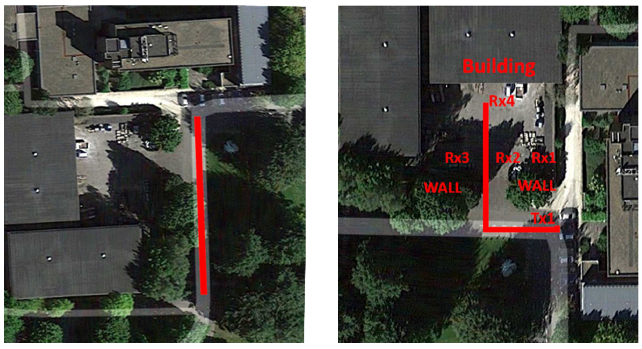

(a) Main road (b) Road and laboratory yard

Fig. 2: Measurement location

The first site is in the neighborhood of UCLouvain campus, in Belgium. The avenue includes two lanes, one for each direction. On the side of road, there are fields of green grass and some trees. During the measurement, the Tx vehicle was traveling on the road while the Rx subject was walking next to the road on a grassy sidewalk. Two types of V2P measurements were carried out, respectively in LoS and partial LoS (cf. Fig. 1). The partial LoS condition is mainly considered there when the Rx subject was walking behind vehicles parked on the road (cf. Fig. 1b). Different mobility patterns were considered including parallel, opposite and orthogonal directions as shown in Fig. 3a where the red and black arrows indicate Tx and Rx movements, respectively. Note that the mobility direction represents the relative mobility between the Tx and Rx.

The second location, also on UCLouvain campus, consists of a main road and a yard in front of a building. The yard is enclosed by walls separated by a car entrance. During the measurement, the Rx subject was walking inside the yard while the Tx vehicle was moving from the main road into the yard or completely within the yard depending on the scenario. Four different scenarios are considered and they are described as follows (cf. Fig. 3b):

- Parallel direction then orthogonal direction 1: Tx and Rx start moving from Tx1 and Rx1, respectively and they meet at Rx2.
- Parallel direction then orthogonal direction 2: Tx vehicle drives from Tx1 to Rx4 while Rx subject walks from Rx1 to Rx3. At this point, it is worth noting that Tx and Rx meet at Rx2 without stopping and then the Rx subject continue crossing behind the mobile vehicle.
- Orthogonal direction then opposite direction: Rx subject walks from Rx4 to Rx2 while Tx vehicle moves from Tx1 to Rx4.
- Convoy direction: Tx and Rx terminals are both moving inside the yard behind each other starting from Rx4 and stopping at Rx2.

The vehicle speed was around 30 km/h except in the convoy direction scenario where the vehicle was moving behind the pedestrian (the vehicle speed was then around the usual walking pedestrian speed, i.e. 5 km/h). The distance between

the Tx vehicle and the Rx pedestrian varied in the range of 2 m to 40 m depending on the measurement scenario.

The measurement campaign was conducted during four days, and a total of 115 measurement runs were recorded. The recorded time was between 3 s and 20 s, approximately, depending on the measurement scenario. Four people were involved in the measurement campaign. In Tx vehicle, one person acted as a driver and a second colleague recorded the Tx GPS information and the car speed. The Rx antenna was carried by a human subject acted as a pedestrian while another person was responsible of controlling the channel sounder and writing the measurement protocol.

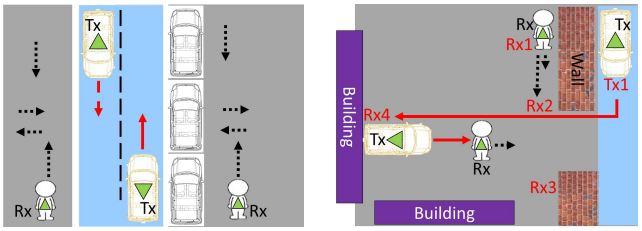

(a) LoS and partial Los scenarios (b) NLoS/LoS scenarios

Fig. 3: Measurement scenarios

III. Channel Modeling Tools

In order to model the mobile-to-mobile (M2M) channels, the non-stationarity of the channel, i.e. the change of channel statistics over time, must be included in the model. In our case, the non-stationarity is due to the dynamic change of the environments around the mobile terminals.

GSCM and non-GSCM approaches were developed in [3], [4], [6] in order to model the V2V channels. Both are defined as a combination of LoS path and secondary MPCs where the channel properties are described statistically. The basic idea is to determine the number of contributed scatterers in each time frame, assign them different channel properties, and sum up their respective signal contributions at the Rx. The non-stationarity is then modeled considering the position change of scatterers around the moving terminals and the birth/death process to account the appearance and disappearance of MPCs through stationary region, for the GSCM and non-GSCM, respectively.

Following their steps, a stochastic channel modeling approach is proposed here in order to model the measurement results. A MPC extraction method and a MPC tracking algorithm are also presented.

A. General channel model

In agreement with our measurement, the time-varying channel impulse response (TVCIR) can be divided into two major parts:

- The first path component represents the shortest detected path and it usually has the highest power with respect to the extracted MPCs. Considering the LoS condition, for instance, the first path component then mainly consists of the LoS and the ground reflection paths (cf. Fig. 7).
- The secondary MPCs stemming from specular reflection of scatterers.

Therefore, the TVCIR can be modeled as follows [4]:

$$h\left(t,\tau\right)=\sum_{p=0}^{P(t)}h_p\left(t,\tau_p\right) \tag{1}$$

where $P(t)$ is the time varying number of discrete scatterers and $p = 0$ represents the first path component. The p-th discrete scatterer contribution can be further modeled as follows [15]:

$$h_p\left(t,\tau_p\right)=\alpha_p(d_p)\delta\left(\tau-\tau_p\right)\delta\left(\varphi^R-\varphi_p^R\right)\delta\left(\varphi^T-\varphi_p^T\right) \tag{2}$$

where $d_p = c \times \tau_p$, $\alpha_p(d_p) = a_p\left(d_p\right)e^{j\phi_p}$, τ_p, φ_p^R and φ_p^T are the time variant propagation distance, complex amplitude, the excess delay and the angles of arrival and departure of the p-th discrete path, respectively. Note that all the discrete multi-path parameters in (2), $a_p e^{j\phi_p}$, τ_p, φ_p^R, φ_p^T are also time variant, although the time dependence is left out to simplify the notations.

B. Detection and tracking algorithms

Detection and tracking algorithms are employed in order to identify the multi-path and the first path components. The extraction procedure is similar to the CLEAN method [16], [17] and it is based on a serial of "search and subtract" of the contributions from the individual discrete scatterers. In order to reduce the chance of detecting noise peaks as MPCs, the algorithm is applied on the power delay profile (PDP) filtered with a 40 λ sliding window [18], assuming vehicle is traveling with an average velocity of 30 km/h as follows:

1) Set the iteration counter $l = 1$ and find for each instant, the delay that corresponds to the maximum PDP amplitude.
2) Store the delay and the amplitude of the detected MPC in two matrices $\mathbf{T}$ and $\mathbf{A}$, respectively.
3) Subtract this dominant peak from the PDP in the delay domain.
4) Set $l = l + 1$ and continue iterate until the maximum detected power amplitude is at least 6 dB above the noise level.

The two resultant matrices $\mathbf{A} \in \mathbb{R}^{L\times N}$ and $\mathbf{T} \in \mathbb{R}^{L\times N}$ are as follows:

$$\mathbf{A}=\begin{bmatrix}\bar{\alpha}_{11} & \bar{\alpha}_{12} & \dots & \bar{\alpha}_{1N}\\ \bar{\alpha}_{21} & \bar{\alpha}_{22} & \dots & \bar{\alpha}_{2N}\\ \vdots & \vdots & \ddots & \vdots\\ \bar{\alpha}_{L1} & \bar{\alpha}_{L2} & \dots & \bar{\alpha}_{LN}\end{bmatrix}\quad \mathbf{T}=\begin{bmatrix}\tau_{11} & \tau_{12} & \dots & \tau_{1N}\\ \tau_{21} & \tau_{22} & \dots & \tau_{2N}\\ \vdots & \vdots & \ddots & \vdots\\ \tau_{L1} & \tau_{L2} & \dots & \tau_{LN}\end{bmatrix} \tag{3}$$

where L is the number of detected discrete MPCs (including the first path elements) and N is the time snapshot number.

Fig. 4 presents the detected discrete contribution of one measured IR when Tx and Rx were in LoS and they were moving in the same direction.

To track the time evolution of the delay and complex amplitude for a detected path, a tracking algorithm similar to the one proposed in [3] is applied. It can be summarized as follows:

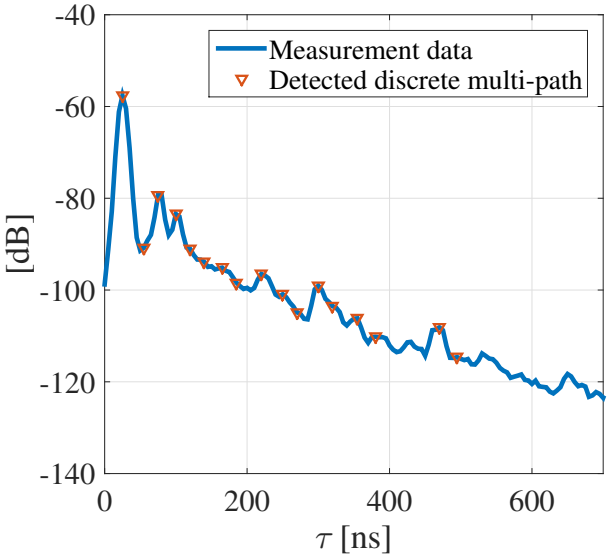

Fig. 4: An example of the outcome of multi-path detection algorithm

1) In order to well estimate the time variation of a path (the tracked curvature), determine the number of time bins N_d used in order to estimate the curvature change over time for the tracked path and the accepted number of time bins N_g during which the components of a tracked path is missing. In our case, N_d and N_g were set to 52.7 λ and 5 λ, respectively, considering the speed of Tx and Rx, the delay and the time resolutions as well as the capability to correctly tracking a path using the proposed algorithm, accordingly.
2) Select a number of MPCs that likely belong to the same discrete scatterer contribution. In other words, the time evolution of their corresponding delay must follow a regression line.
3) Store the tracked delay components in matrix $\mathbf{T_f}$, then remove the tracked components from $\mathbf{A}$ and $\mathbf{T}$ by setting the appropriate entries to 0.
4) Iterate until no additional discrete scatterer contribution is in $\mathbf{A}$ ($\mathbf{T}$).

Finally, the tracked paths that have a time appearance longest than 40λ were only considered. This was done in order to better model the tracked path, in other words to correctly estimate the model parameters as will be described in the following section. Moreover, for each instant, the measured complex amplitudes α_p that correspond to the appropriate delay values in $\mathbf{T_f}$ are stored in the matrix $\mathbf{A_f}$.

Consequently the matrices $\mathbf{T}_f \in \mathbb{R}^{P\times N}$ and $\mathbf{A}_f \in \mathbb{C}^{P\times N}$ represent the evolution of the detected MPCs (including the first path component) in time (τ_p) and in complex amplitude (α_p), respectively.

Fig. 5 and Fig. 6 show a good agreement between the measured PDP and the tracking outcome considering different mobility patterns under the LoS, partial LoS or the NLoS/LoS conditions. The partial LoS scenarios are considered here when Rx was moving behind parked vehicles while the NLoS/LoS scenarios describe the scenarios measured in the second location where the Tx was moving from the main road to the yard to encounter the Rx (cf. Fig. 3).

At this point it is worth noting that some similar scatterers are tracked in the orthogonal direction scenarios for both orientations considering a given propagation condition (cf. Fig. 5b and Fig. 5c). For example, in LoS condition, the MPCs that are moving in parallel with respect to first path, are shown in both cases: towards each other and faraway from each other. Therefore, it can be assumed that they come from same scatterers. Moreover, we can also presume that the path detected between 300 ns and 400 ns at 0 s and tracked to 400 ns approximately after 4 s, shown in Fig. 5b, is the same one that has a delay of 400 ns for a time of 0 s and a delay between 300 ns and 400 ns around 4 s, as observed in Fig. 5c. In fact, under a perfect scenario measurement conditions and same propagation condition, one can expect to obtain in both orientations of the orthogonal direction scenarios, two PDPs such as one is the mirror of the other. Nevertheless, this comparison was given to show the significance of the results given by the tracking algorithm.

Looking into the PDPs given by NLoS/LoS scenarios (cf. Fig. 6a and Fig. 6b), one can see the power variation of the first path power due to the change of propagation conditions: from NLoS, where the direct path was mainly blocked by walls (in this case Tx and Rx were unable to see each other), to LoS where Tx and Rx were moving in the same location close to each other. Therefore, these power variation is modeled based on the environment condition and the transition region as explained in the next section.

IV. Channel Modeling Results

Similar to [3], [4], the time variant complex amplitude of the p-th MPC presented in (2) is modeled as:

$$\alpha_p = \sqrt{G_p} g_p e^{j\phi_p} \tag{4}$$

where $\sqrt{G_p}$ and $g_p e^{j\phi_p}$ are the time variant power averaged over small-scale fading and the small-scale fading of the p-th MPC, respectively.

The first arriving path mainly consists of the LoS and the ground reflection path. Hence, it exhibits fading characteristics and it is modeled in the same way by replacing the index p by 0 in (4).

The time-variant power averaged over the small-scale fading is modeled as follows:

$$10\log_{10} G_p = -\left[PL_p + S_p\right] \tag{5}$$

where PL_p and S_p are the PL and the large-scale fading, respectively.

Depending on the environment propagation condition (i.e. LoS, partial LoS, partial NLoS, NLoS), the measurement data were aggregated in order to extract the best fitting values of PL, large- and small-scale fading parameters. In this section, the PL, small- and large-scale fading models are presented for the first path component and secondary MPCs. Table II reports the model parameters.

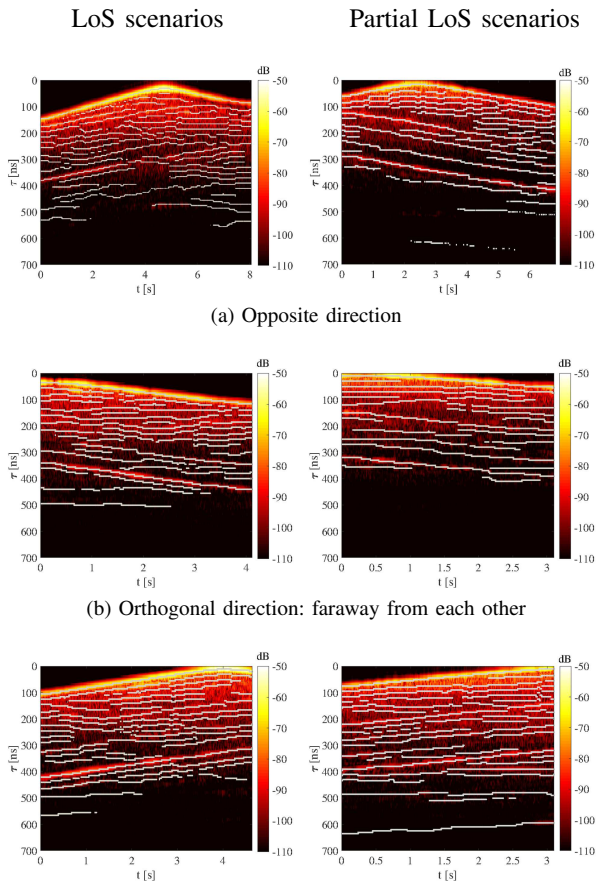

(a) Opposite direction

(b) Orthogonal direction: faraway from each other

(c) Orthogonal direction: towards each other

Fig. 5: Measured PDP vs. the outcome of MPC tracking algorithm (grey line) for different mobility patterns under the LoS and partial LoS conditions

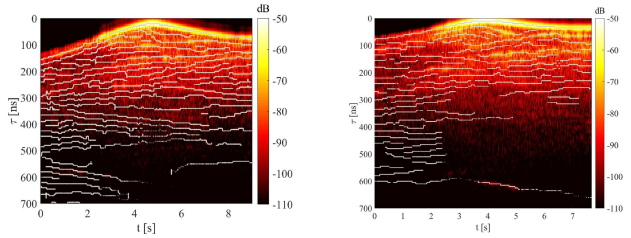

(a) Orthogonal direction then opposite direction

(b) parallel direction then orthogonal direction 2

Fig. 6: Measured PDP vs. the outcome of MPC tracking algorithm (grey line) for different mobility patterns under the LoS/NLoS condition

A. Path loss model

1) First path component: For LoS scenarios, the PL is modeled with a two rays model defined as follows [19]:

$$PL_0 = \left[10 \log_{10} \left(\frac{\lambda}{4\pi} \right)^2 \left| \frac{e^{-\frac{2\pi i d_0}{\lambda}}}{d_0} + \Gamma_R \frac{e^{-\frac{2\pi i d_g}{\lambda}}}{d_g} \right|^2 \right] \quad (6)$$

where d_0 is the LoS distance, d_g is the path distance between the Tx reflected off the ground to the Rx and Γ_R is the Fresnel

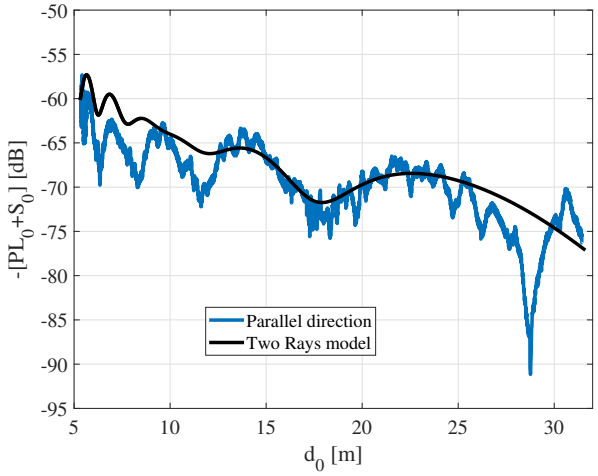

Fig. 7: Example of PL modeling of the first path component for LoS scenarios

reflection coefficient given as:

$$\Gamma_R = \frac{\epsilon_g \sin\theta - \sqrt{\cos\theta^2 - \epsilon_g}}{\epsilon_g \sin\theta + \sqrt{\cos\theta^2 - \epsilon_g}} \quad (7)$$

where θ is the angle between the reflected path and ground plane and ϵ_g is the relative dielectric constant expressed as $\beta - j60\sigma\lambda$. β and σ are the relative permittivity and conductivity and they are set based on [20, Figure 14], considering a medium dry ground, to 15 and 0.35 S/m respectively.

Fig. 7 presents an example of PL extracted from the first path component measured in LoS scenario and the proposed two rays model. As seen, the measured PL is in line with the two rays model. Note that the misalignment is due to the parameter estimations, i.e. dielectric constant, reflected and direct path distances. The Kullback divergence metric [21] was used to quantify the dispersion between the model and the measurement, i.e. how far the model moves away from the measurement, as follows:

$$KD = \sum_t \left(\widehat{PL_0} - \widetilde{PL_0} \right) log_{10} \frac{\widehat{PL_0}}{\widetilde{PL_0}} \quad (8)$$

where $\widetilde{PL_0}$ is the PL model and the $\widehat{PL_0}$ is the amplitude of the first path.

The mean value of the Kullback divergence was calculated as the absolute average over all the results obtained from different runs in LoS, and it was equal to 0.0014. this value is close to zero indicating the convergence of the model towards representing the measurement behavior.

By filtering the amplitude $|\alpha_0(d_0)|^2$ with a rectangular sliding window of 40λ assuming 30 km/h the Tx vehicle speed, the time variant power averaged over the small-scale fading is extracted in partial LoS scenarios and NLoS/LoS scenarios. Then, the large-scale fading and the PL are separated by deriving a PL law. Note that the 40λ corresponds to a distance of 3 m approximately during 0.38 s. A careful selection of the window size is critical to avoid having noisy components appropriate to the small-scale fading components and to apply

the average filter over uncorrelated data samples. In the literature, it was mostly considered in the range of 20λ and 40λ both for Ultra-high frequency (UHF) and Very-high frequency (VHF) [18].

The logarithmic PL model is used for the partial LoS scenarios and it is expressed as follows:

$$PL_0 = PL_{0,ref} + 10n_0 \log_{10}\left(\frac{d_0}{d_{0,ref}}\right) \quad (9)$$

where $PL_{0,ref}$ and n_0 are the PL at reference distance $d_{0,ref}$ that is equal to 1 m and the PL exponent, respectively.

Fig. 8 shows a good agreement between the proposed model and the measurement data. The mean value of the Kullback divergence was equal to 0.0017.

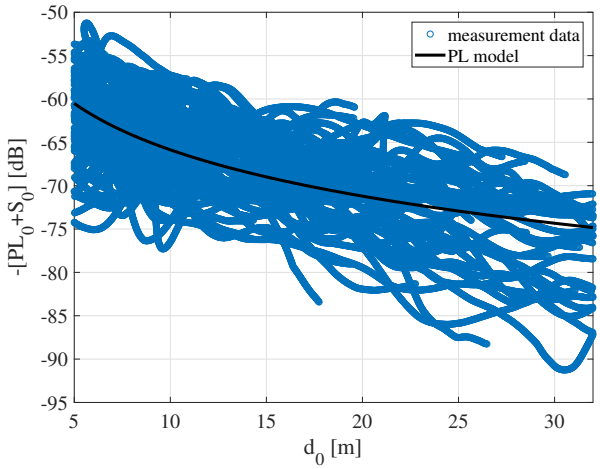

Fig. 8: PL model of the First path component measured in parial LoS scenarios

Due to the transition from NLoS to LoS in scenarios described in Fig. 3b, a PL model is developed and it consists of a system of three equations in order to represent the following regions:

- LoS region, where Tx and Rx are in LoS.
- NLoS region, where Tx and Rx are in NLoS due to wall blocking the direct path.
- Transition region, i.e. partial NLoS that connects the two previous regions and it was characterized by a steep decrease (or increase) of the channel gain.

Therefore, the proposed PL model was expressed as follows:

$$PL_0 = \begin{cases} PL_{0,ref}^{NLoS} + 10n_0^{NLoS}\log_{10}\frac{d_0}{d_{0,ref}} & d_{NLoS} \leq d_0 \\ PL_{0,ref}^{NLoS/LoS} + n_0^{NLoS/LoS} \times d_0 & d_{NLoS} \leq d_0 \leq d_{LoS} \\ PL_{0,ref}^{LoS} + 10n_0^{LoS}\log_{10}\frac{d_0}{d_{0,ref}} & d_0 \leq d_{LoS} \end{cases} \quad (10)$$

where $PL_{0,ref}^{NLoS}$, $PL_{0,ref}^{NLoS}$, n_0^{NLoS}, n_0^{LoS} are the PL at reference distance $d_{0,ref}$ and the PL exponents given when Tx and Rx are in NLoS and LoS, respectively. d_{NLoS} and d_{LoS} represent the critical distance between terminals indicating the end of NLoS and LoS conditions, respectively. $PL_{0,ref}^{NLoS/LoS}$ and $n_0^{NLoS/LoS}$ are the parameters of the PL equation depicting the losses during the transition region (between the LoS and NLoS) when the direct link between Tx and Rx swaps from NLoS to LoS. Note that the proposed model is an empirical model that was obtained to depict the measured PL shape.

In order to determine the critical distance d_{NLoS} and d_{LoS}, the GPS coordinate of a point, says "O", between the two walls as shown in Fig. 9 was estimated using Google maps. Then, the distances from this point to Tx and Rx were calculated considering the Tx and Rx GPS coordinates. The Tx GPS was stored during measurement while the Rx GPS was estimated using Google map.

The distances from the point O to Tx and Rx are denoted by $\overline{OT_x}$ and $\overline{OR_x}$, respectively and their values were assigned with negative and positive signs depending on the Tx and Rx positions with respect to O as follows:

- If Tx is on the road, a negative sign is assigned to $\overline{OT_x}$.
- If Tx is inside the yard, a positive sign is assigned to $\overline{OT_x}$.
- If Rx is on the right side of O, a negative sign is assigned to $\overline{OR_x}$.
- If Rx is on the left side of O, a positive sign is assigned to $\overline{OR_x}$.

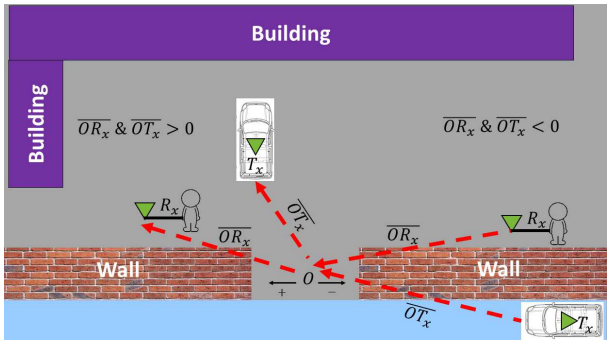

Fig. 9: Method to separate LoS from NLoS in the NLoS/LoS scenarios

This method was used to define the three regions, i.e. LoS, NLoS and transition region. For instance, if $\overline{OT_x}$ is negative, then Tx is on the road and the terminals can be subject to the NLoS condition or the transition region based on the $\overline{OT_x}$ value. If Tx approaches the car entrance, then $\overline{OT_x}$ will be close to zero, and the terminal links are considered in the transition region. In the scenario of parallel direction then orthogonal direction 2, the positive sign of $\overline{OR_x}$ distance defines the LoS region because it indicates when Rx is traversing to the next side of the yard. Note in this case, the $\overline{OT_x}$ value was also positive.

Fig. 10 presents a good agreement between the proposed model and the two NLoS/LoS measurement scenarios, the Kullback divergence metric gives a dispersion of 0.0018 indicating the capacity of model to depict the measurement behavior. At this point it is worth noting that the measurement was uncontrollable since Tx and Rx cannot see each other during the beginning of the measurements, therefore a transition region of one realization can belong to the LoS or NLoS regions for other realizations which explains the mixing regions (cf. Fig. 10a). For the orthogonal then opposite direction scenario, a transition region was not clearly noticed from the measurement data, so only the LoS and NLoS equations

were used (cf. Fig. 10b). Therefore, more measurement are requested and a further investigation is required to properly model this type of scenarios.

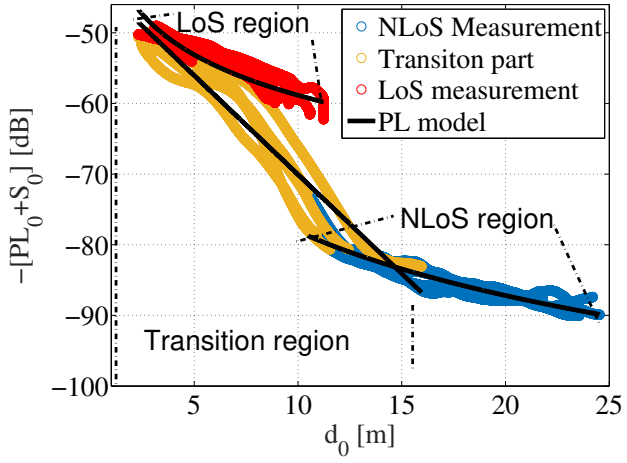

(a) Parallel then orthogonal direction

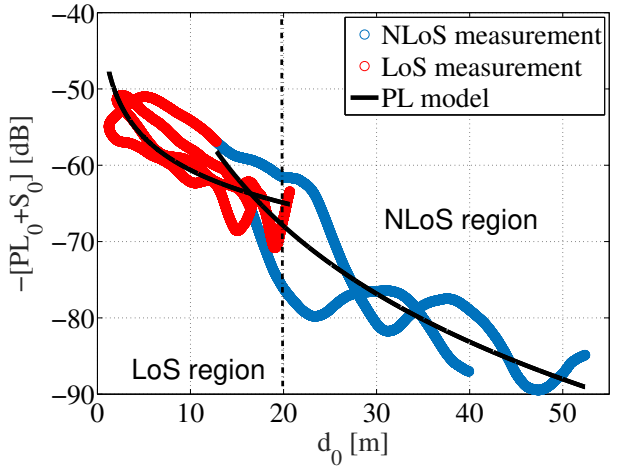

(b) Orthogonal then opposite direction

Fig. 10: First path component: PL model vs. measurement data considering the NLoS/LoS scenarios

2) Secondary multi-path components: Similar to the previous section, the time average power is extracted by filtering the amplitude $|\alpha_p(d_p)|^2$ with a time domain rectangular sliding window of $40\,\lambda$ [18]. The following step is to separate the large-scale fading and the PL by deriving a PL law as follows:

$$PL_p = PL_{p,ref} + 10 n_p \log_{10}(d_p/d_{p,ref}) \qquad (11)$$

where $PL_{p,ref}$ and n_p represent the PL at reference distance of $d_{p,ref}$ which is equal to 1 m and the PL exponent, respectively.

Depending on the scenario propagation condition, the measurement data were interpolated in order to extract the best fitting values of n_p and $PL_{0,p}$. Note that similarities in terms of n_p and $PL_{p,ref}$ for LoS and NLoS scenarios are expected since both measurements were done in the same location (cf. Table II). Note that the path loss parameters values obtained for the first path and multi-path components are similar to the ones given in V2V propagation measurements for similar environment [3], [4], [22].

B. Large-scale fading

1) First path component: After subtracting the losses from the first path component using equation (6), (9) and (10) depending on the measurement propagation conditions and filtering out the small-scale fading, the large-scale fading was then characterized by a normal distribution in dB of zero mean and an auto-correlation (ACF) described as follows:

$$R_{S,0}(\Delta t) = \sigma_{S,0}^2 e^{-\ln 2 \times \left(\frac{\Delta t}{t_{c,0}}\right)^2} \qquad (12)$$

where $\sigma_{S,0}$ and $t_{c,0}$ are the standard deviation and the coherence time at 0.5, respectively.

Note that the standard deviation of the large-scale fading given in LoS and partial LoS scenarios are approximately the same, as expected.

2) Secondary multi-path components: The large-scale fading of the discrete scatterers was deduced after derived the PL law (11) and it was modeled by a normal distribution in dB of zero mean and an ACF described by an exponential decay law as follows:

$$R_{S,p}(\Delta t) = \sigma_{S,p}^2 e^{-\ln 2 \Delta t/(t_{c,p})} \qquad (13)$$

where $\sigma_{S,p}$ and $t_{c,p}$ are the standard deviation and the coherence time at 0.5, respectively.

The standard deviation $\sigma_{S,p}$ measured in the three different conditions, are also approximately similar, as the measurement were conducted in places nearby so the same scatterer contributions are expected.

C. Small-scale fading

The small-scale fading envelope corresponds to the filtered out signal when performing the 40λ sliding average window on power amplitude of discrete scatterers $|\alpha_p(d_p)|^2$ or first path contributions $|\alpha_0(d_0)|^2$. It was characterized for both by Rice distribution.

1) First path component: Considering the propagation condition, the first path small-scale fading is modeled with a Rice distribution that has a K-factor $K_{F,0}$ and a standard deviation $\sigma_{F,0}$ (cf. Fig. 11).

Note that the standard deviation $\sigma_{F,0}$ given in partial LoS scenarios is slightly larger than the one extracted from the LoS measurements due to the presence of parked vehicle shadowing the LoS path (cf. Table II).

In fact, as seen in Fig. 12, the first path power fluctuates rapidly in the partial LoS scenarios compared to the LoS scenarios. A deep fade of -90 dB occurred in partial LoS and this can be due to the shadowing of vehicles while the minimum power obtained from the LoS scenarios is around -75 dB.

The Rice parameters extracted from the NLoS/LoS measurement scenario have shown a slight variation with respect to the relative distance between terminals (cf. Fig. 11c and

TABLE II: Parameters of the first path component and secondary MPCs in LoS, partial LoS and NLoS/LoS scenarios

			LoS scenarios	partial LoS scenarios	NLoS/LoS scenarios	
					PO scenario* NLoS/transition/LoS	OO scenario* NLoS/transition/LoS
First path	Path loss	n_0	-	1.78	3/2.8/1.9	5.2/-/1.3
		PL_0[dB]	-	48	48/42/40	53/-/2.5
	Large-scale fading	$\sigma_{S,0}$ [dB]	3.87	4.92	1.77	4.176
		$t_{c,0}$ [s]	0.48	0.67	0.34	0.55
	Small-scale fading	$K_{F,0}$ [dB]	11.058	8.52	cf. (14)&(15)	cf.(16)
		$\sigma_{F,0}$	0.2	0.26	cf. (15)	cf. (16)
Secondary multi-path	Path loss	n_p	3.38	3	4.13	
		PL_p[dB]	36.75	43.4	19.65	
	Large-scale fading	$\sigma_{S,p}$ [dB]	4.67	4.68	4.91	
		$t_{c,p}$ [s]	1	1.26	1.7	
	Small-scale fading	$K_{F,p}$ [dB]	0.25	-0.2	-0.85	
		$\sigma_{F,p}$	0.61	0.63	0.66	

*PO scenario: parallel then orthogonal walking direction; OO scenario: Orthogonal then opposite walking direction.

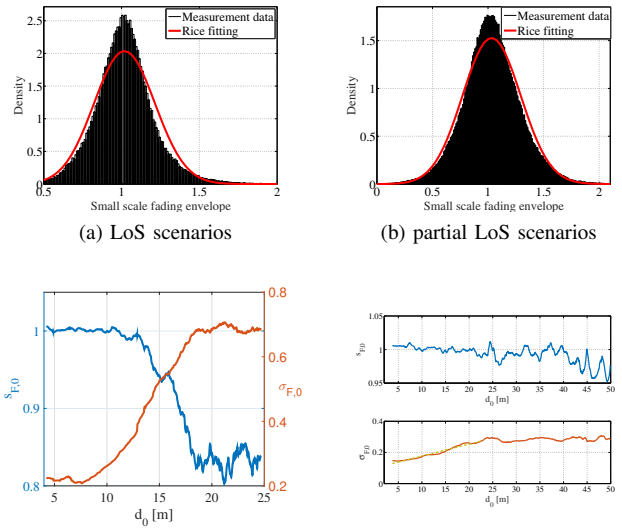

(a) LoS scenarios (b) partial LoS scenarios

(c) Parallel then orthogonal (d) Orthogonal then opposite

Fig. 11: First path component: small-scale fading distribution

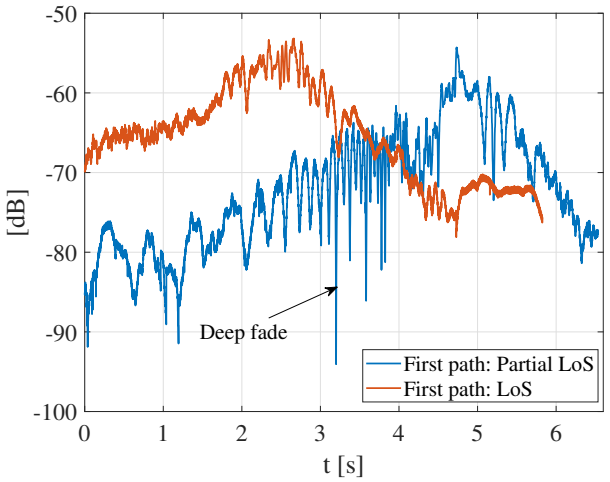

Fig. 12: First path component: NLoS vs. LoS

Fig. 11d). This variation is due to the environment mutation from NLoS to LoS. Note that the three defined regions, i.e. LoS, NLoS and transition regions, detected in the PL of the first path component measured in NLoS/Los scenarios can be also seen here for parallel then orthogonal walking scenarios.

Therefore, for the parallel then orthogonal walking directions, the non-centrality parameters $s_{F,0}$ and the standard deviation $\sigma_{F,0}$ were modeled as follows:

$$s_{F,0} = \begin{cases} 1 & d_0 < 13.5 \\ -0.03d_0 + 1.4 & 13.5 \leq d_0 \leq 18.16 \\ 0.83 & d_0 \geq 18.16 \end{cases} \quad (14)$$

$$\sigma_{F,0} = \begin{cases} 0.22 & d_0 < 10 \\ 0.053d_0 - 0.29 & 10 \leq d_0 \leq 18.7 \\ 0.7 & d_0 \geq 18.7 \end{cases} \quad (15)$$

For the orthogonal then opposite walking scenarios, $s_{F,0}$ is always approximately equal to 1 while $\sigma_{F,0}$ increases slightly with distance until 20 m as follows:

$$\sigma_{F,0} = \begin{cases} 7.7 \times 10^{-3} d_0 + 0.1 & d_0 < 20 \\ 0.27 & d_0 \geq 20 \end{cases} \quad (16)$$

2) Secondary multi-path components: Fig. 13 presents a good agreement between the measured small-scale fading of the secondary MPCs and the Rice distribution for the different measurement scenarios. For a given propagation environment, all the extracted MPCs were concatenated in order to compute the Rice parameters. Note that the Rice parameters are similar for all measurements, this can be reasonably explained by the fact that the measurements were conducted in the same location so similar discrete scatterer contributions were expected. The K-factors are close to 0 dB which results in a Rayleigh distribution.

V. Conclusion

Due to the lack of V2P channel measurement, characterization and modeling, we present in this paper, for the first time, wide-band measurement based V2P channel characterization and modeling. The full description of the measurement campaign was provided. The measurements were performed at 3.8 GHz within a bandwidth of 200 MHz. The peculiarity of this frequency band is its proximity to the 3.5 GHz, which

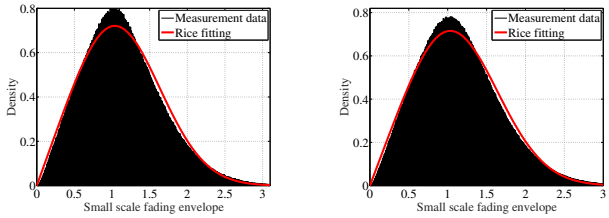

(a) LoS scenarios (b) NLoS scenarios

Fig. 13: Secondary MPCs: small-scale fading distributions

is considered for 5G network. Different mobility patterns were considered in various propagation environments, i.e. LoS, partial LoS (obstructed LoS) where the pedestrian was walking behind parked vehicles and the NLoS/LoS where the V2P link passes trough three stages, i.e. the direct path blocked by wall separating terminals, a transition phase from NLoS to LoS and the LoS phase. Extension of the model for V2P channel scenarios including moving vehicles and mutiple antennas is left for further works.

While the obstructed LoS scenarios can degrade the received signal power, the NLoS/LoS scenarios occur mostly in the safety critical scenarios such as crossing street intersections. A stochastic channel modeling approach similar to the one proposed for V2V channels [3], [4] is proposed and it consists of two major components: the first path component and the secondary MPCs. A detection and tracking algorithms are implemented in order to track the first path component and the discrete scatterer MPCs over time. They are best fitted with a combination of PL, large-scale fading and small-scale fading. Depending on the measurement propagation condition (LoS, partial LoS, partial NLoS and NLoS/LoS), the parameter values are given. The small-scale fading was found to be described with a Rice distribution while the large-scale fading was characterized in dB by a normal distribution with zero mean. Depending on the measurement scenario, a PL model for the first path component was proposed while a log distance model was always used for the MPCs. Therefore, a two rays model was implemented for the PL of the first path component in LoS scenarios and a log distance model for the partial LoS scenarios. In the NLoS/LoS scenarios, a model based on three equations was proposed in order to present the LoS, NLoS and the partial NLoS regions. Moreover, the Rice parameters of the first path components for this type of scenarios were exhibited a variation in function of the Tx-Rx distance, highlighting the non-stationary behavior of the V2P fading channel.

This model can be used to depict the V2P channel characteristics considering the scatterer density and distribution which can be obtained geometrically from the measurement locations or statistically based on the MPCs extracted from the tracking algorithm. In both methods, the non-stationarity behavior of the channel will be characterized due to the dynamic change of the scatterers around the moving terminals. Therefore, future works include the implementation of the model based on the given scenario and the propagation condition with fading characteristics including the Doppler characteristics.

ACKNOWLEDGMENT

The authors would like to thank T. Pairon, Y. Miao, Y. Pan and Q. Gueuning for their help in the measurement campaign.

REFERENCES

[1] *Draft Amendment to Wireless LAN Medium Access Control (MAC) and Physical Layer (PHY) Specifications: Wireless Access in Vehicular Environment*, Jan 2006. IEEE P802.11p/D0.26.

[2] D. Bezzina, "Light vehicle platform update," Apr. 2008. [Public Meeting].

[3] J. Karedal, F. Tufvesson, N. Czink, A. Paier, C. Dumard, T. Zemen, C. F. Mecklenbrauker, and A. F. Molisch, "A geometry-based stochastic mimo model for vehicle-to-vehicle communications," *IEEE Transactions on Wireless Communications*, vol. 8, no. 7, pp. 3646–3657, 2009.

[4] O. Renaudin, V. M. Kolmonen, P. Vainikainen, and C. Oestges, "Wide-band measurement-based modeling of inter-vehicle channels in the 5-ghz band," *IEEE Transactions on Vehicular Technology*, vol. 62, pp. 3531–3540, Oct 2013.

[5] I. Sen and D. W. Matolak, "Vehicle–vehicle channel models for the 5-ghz band," *IEEE Transactions on Intelligent Transportation Systems*, vol. 9, no. 2, pp. 235–245, 2008.

[6] R. He, O. Renaudin, V.-M. Kolmonen, K. Haneda, Z. Zhong, B. Ai, and C. Oestges, "A dynamic wideband directional channel model for vehicle-to-vehicle communications," *IEEE Transactions on Industrial Electronics*, vol. 62, no. 12, pp. 7870–7882, 2015.

[7] Y. Ibdah and Y. Ding, "Mobile-to-mobile channel measurements at 1.85 ghz in suburban environments," *IEEE Transactions on Communications*, vol. 63, pp. 466–475, Feb 2015.

[8] M. G. Doone and S. L. Cotton, "First-order characteristics of the person-to-vehicle channel at 5.8 ghz," in *The 8th European Conference on Antennas and Propagation (EuCAP 2014)*, pp. 848–851, April 2014.

[9] M. G. Doone and S. L. Cotton, "Fading characteristics of dynamic person-to-vehicle channels at 5.8 ghz," in *2015 9th European Conference on Antennas and Propagation (EuCAP)*, pp. 1–5, May 2015.

[10] S. Bauk, J. A. L. Calvo, R. Mathar, and A. Schmeink, "V2p/i communication for increasing occupational safety at a seaport," in *2017 International Symposium ELMAR*, pp. 79–82, Sept 2017.

[11] X. Wu, R. Miucic, S. Yang, S. Al-Stouhi, J. Misener, S. Bai, and W. h. Chan, "Cars talk to phones: A dsrc based vehicle-pedestrian safety system," in *2014 IEEE 80th Vehicular Technology Conference (VTC2014-Fall)*, pp. 1–7, Sept 2014.

[12] I. Rashdan, F. de Ponte Mller, W. Wang, M. Schmidhammer, and S. Sand, "Vehicle-to-pedestrian channel characterization: Wideband measurement campaign and first results," in *12th European Conference on Antennas and Propagation (EuCAP 2018)*, pp. 1–5, April 2018.

[13] G. Makhoul, R. D'Errico, and C. Oestges, "Wideband vehicle to pedestrian propagation channel characterization and modeling," in *12th European Conference on Antennas and Propagation (EuCAP 2018)*, pp. 1–4, April 2018.

[14] M. Boban, R. Meireles, J. Barros, P. Steenkiste, and O. K. Tonguz, "Tvrtall vehicle relaying in vehicular networks," *IEEE Transactions on Mobile Computing*, vol. 13, pp. 1118–1131, May 2014.

[15] A. F. Molisch, "A generic model for mimo wireless propagation channels in macro- and microcells," *IEEE Transactions on Signal Processing*, vol. 52, pp. 61–71, Jan 2004.

[16] R.-M. Cramer, R. A. Scholtz, and M. Z. Win, "Evaluation of an ultra-wide-band propagation channel," *IEEE Transactions on Antennas and Propagation*, vol. 50, no. 5, pp. 561–570, 2002.

[17] U. Schwarz, "Mathematical-statistical description of the iterative beam removing technique (method clean)," *Astronomy and Astrophysics*, vol. 65, p. 345, 1978.

[18] W. C. Y. Lee, "Estimate of local average power of a mobile radio signal," *IEEE Transactions on Vehicular Technology*, vol. 34, pp. 22–27, Feb 1985.

[19] H. Xia, H. L. Bertoni, L. R. Maciel, A. Lindsay-Stewart, and R. Rowe, "Radio propagation characteristics for line-of-sight microcellular and personal communications," *IEEE Transactions on Antennas and Propagation*, vol. 41, no. 10, pp. 1439–1447, 1993.

[20] Recommendation ITU-R P.527-4, *Electrical characteristics of the surface of the earth*. Geneva: Electronic publication, 2017.

[21] M. Basseville, "Distance measures for signal processing and pattern recognition," *Signal processing*, vol. 18, no. 4, pp. 349–369, 1989.

[22] J. Karedal, N. Czink, A. Paier, F. Tufvesson, and A. F. Molisch, "Path loss modeling for vehicle-to-vehicle communications," *IEEE Transactions on Vehicular Technology*, vol. 60, pp. 323–328, Jan 2011.